

# Conformational heterogeneity of molecules physisorbed on a gold surface at room temperature

Mingu Kang<sup>1,2</sup>, Hyunwoo Kim<sup>3</sup>, Elham Oleiki<sup>4</sup>, Yeonjeong  
Koo<sup>1,2</sup>, Hyeongwoo Lee<sup>1,2</sup>, Huitae Joo<sup>2</sup>, Jinseong  
Choi<sup>2</sup>, Taeyong Eom<sup>5</sup>, Geunsik Lee<sup>4</sup>, Yung Doug Suh<sup>3,6\*</sup>  
and Kyoung-Duck Park<sup>1,2\*</sup>

<sup>1</sup>Department of Physics, Pohang University of Science and Technology (POSTECH), 77, Cheongam-ro, Pohang, 37673, Republic of Korea.

<sup>2</sup>Department of Physics, Ulsan National Institute of Science and Technology (UNIST), 50, UNIST-gil, Ulsan, 44919, Republic of Korea.

<sup>3</sup>Laboratory for Advanced Molecular Probing (LAMP), Korea Research Institute of Chemical Technology (KRICT), 141, Gajeong-ro, Daejeon, 34114, Republic of Korea.

<sup>4</sup>Department of Chemistry, Ulsan National Institute of Science and Technology (UNIST), 50, UNIST-gil, Ulsan, 44919, Republic of Korea.

<sup>5</sup>Thin Film Materials Research Center, Korea Research Institute of Chemical Technology (KRICT), 141, Gajeong-ro, Daejeon, 34114, Republic of Korea.

<sup>6</sup>Department of Chemistry and School of Energy and Chemical Engineering, Ulsan National Institute of Science and Technology (UNIST), 50, UNIST-gil, Ulsan, 44919, Republic of Korea.

\*Corresponding author(s). E-mail(s): [ydoughsuh@gmail.com](mailto:ydoughsuh@gmail.com);  
[parklab@postech.ac.kr](mailto:parklab@postech.ac.kr);

Contributing authors: [mkgang96@postech.ac.kr](mailto:mkgang96@postech.ac.kr); [hwkim@kRICT.re.kr](mailto:hwkim@kRICT.re.kr);  
[elham1368@unist.ac.kr](mailto:elham1368@unist.ac.kr); [yjkoo@postech.ac.kr](mailto:yjkoo@postech.ac.kr);  
[physicsurf@postech.ac.kr](mailto:physicsurf@postech.ac.kr); [htlv010@unist.ac.kr](mailto:htlv010@unist.ac.kr);  
[chlwlstjd200@unist.ac.kr](mailto:chlwlstjd200@unist.ac.kr); [eomt@kRICT.re.kr](mailto:eomt@kRICT.re.kr); [gslee@unist.ac.kr](mailto:gslee@unist.ac.kr);

### Abstract

A quantitative single-molecule tip-enhanced Raman spectroscopy (TERS) study at room temperature remained a challenge due to the rapid structural dynamics of molecules exposed to air. Here, we demonstrate the hyperspectral TERS imaging of single or a few brilliant cresyl blue (BCB) molecules at room temperature, along with quantitative spectral analyses. Robust chemical imaging is enabled by the freeze-frame approach using a thin Al<sub>2</sub>O<sub>3</sub> capping layer, which suppresses spectral diffusions and inhibits chemical reactions and contaminations in air. For the molecules resolved spatially in the TERS image, a clear Raman peak variation up to 7.5 cm<sup>-1</sup> is observed, which cannot be found in molecular ensembles. From density functional theory-based quantitative analyses of the varied TERS peaks, we reveal the conformational heterogeneity at the single-molecule level. This work provides a facile way to investigate the single-molecule properties in interacting media, expanding the scope of single-molecule vibrational spectroscopy studies.

**Keywords:** Conformational heterogeneity, Freeze-frame, Single-molecule studies, Tip-enhanced Raman spectroscopy (TERS), Vibrational spectroscopy

## Introduction

Observations of single molecules in different chemical environments<sup>1–11</sup> are enabled via surface-enhanced Raman scattering (SERS) or tip-enhanced Raman spectroscopy (TERS), based on their characteristic spectral “fingerprint.”<sup>12–15</sup> In general, SERS provides larger enhancement factor in single-molecule detection compared to TERS<sup>16</sup> which gives access to extremely weak vibrational responses of single-molecules.<sup>17</sup> On the other hand, TERS allows to probe even individual chemical bonds in a single-molecule<sup>18–21</sup> using a strongly localized optical field at the plasmonic nano-tip,<sup>22–24</sup> controlled by scanning probe microscopy approaches.<sup>16,25</sup>

Specifically, these experiments revealed the conformational heterogeneity, intramolecular coupling, vibrational dephasing, and molecular motion of single molecules at cryogenic temperatures under ultrahigh vacuum (UHV) environments.<sup>5,18,26–28</sup> The extreme experimental conditions are advantageous to reduce rotational and spectral diffusions of single molecules and prevent contamination of tips from a surrounding medium. On the other hand, the cryogenic TERS setup cannot be widely deployable because its configuration is highly complicated and the level of difficulty for experiments is also very high. Moreover, performing single-molecule TERS experiments at room temperature is necessarily required to investigate the molecular functions and interactions with respect to chemical environments, such as temperature and atmospheric condition.<sup>5,29,30</sup>

In particular, understanding the conformational heterogeneity of single molecules in the non-equilibrium state is highly desirable because it can address many fundamental questions regarding the structure and function of many biological systems,<sup>31–35</sup> such as protein folding<sup>36,37</sup> and RNA dynamics.<sup>38–40</sup> Previously, a few TERS groups technically detected single molecules at room temperature,<sup>30,41,42</sup> yet

only limited molecular properties were characterized due to the rapid structural dynamics of molecules exposed to air. Therefore, a systematic approach for robust single-molecule TERS experiments at room temperature is highly desirable.

Here, we present a room-temperature freeze-frame approach for single-molecule TERS. To capture the single molecules, we deposit an atomically thin dielectric capping layer (0.5 nm thick Al<sub>2</sub>O<sub>3</sub>) onto the molecules on the metal substrate. The capping layer not only provides a freeze-frame for individual molecules, but also protects them from unwanted chemical contaminations under ambient conditions, especially by sulfur<sup>43</sup> and carbon<sup>44</sup> molecules. Furthermore, it could prevent the sample molecules from getting picked up by the tip during the scanning. The freeze-frame also keeps the molecules stable at a single-position with much less molecular motions, and thus enables robust single-molecule level TERS experiments at room temperature. Through this approach, we obtain TERS maps of single-level brilliant cresyl blue (BCB) molecules at room temperature for the first time, allowing to probe the spatial heterogeneity of the single BCB molecules adsorbed on the Au surface. Furthermore, through the quantitative analysis of the measured TERS frequency variation through density functional theory (DFT) calculations, we provide a comprehensive picture of the conformational heterogeneity of single molecules at room temperature.

## Results and discussion

**Pre-characterization for ideal TERS conditions.** For highly sensitive single-molecule level detection at room temperature, we use the bottom-illumination mode TERS, as illustrated in Fig. 1a. As a sample system, BCB molecules were spin-coated on the thin metal film and covered by an Al<sub>2</sub>O<sub>3</sub> capping layer to suppress rotational and spectral diffusions.<sup>5</sup> Note that a previous study demonstrated that photobleaching of BCB molecules is significantly reduced under vacuum environment compared to the ambient condition because oxygens in air cause the photodecomposition process.<sup>30</sup> Hence, the Al<sub>2</sub>O<sub>3</sub> capping layer is beneficial to reduce the photobleaching effect of molecules in our experiment. Moreover, this capping layer maintains the molecules immobile and prevent possible contaminations of the Au tip, e.g., adsorption of the probing molecules on to the tip surface that can cause artifact signals, as shown in Fig. 1a (see Fig. S1 for more details). We used an electrochemically etched Au tip attached to a tuning fork for normal-mode atomic force microscopy (AFM) operation (see Methods for details). Using an oil-immersion lens (NA = 1.30), we could obtain a focused excitation beam with a sub-wavelength scale, which can highly reduce the background noise of far-field signals in TERS measurements.

Furthermore, in combination with the radially polarized excitation beam, we achieved strong field localization in the normal direction with respect to the sample surface, i.e., a strong out-of-plane excitation field in parallel with the tip axis.<sup>45,46</sup> The excitation field, with a wavelength of 632.8 nm, is localized at the nanoscale tip apex, and the induced plasmon response gives rise to the resonance Raman scattering effect with the BCB molecules.<sup>41</sup> Fig. 1b shows the far-field and TERS spectra of BCB molecules measured with linearly and radially polarized excitation beams

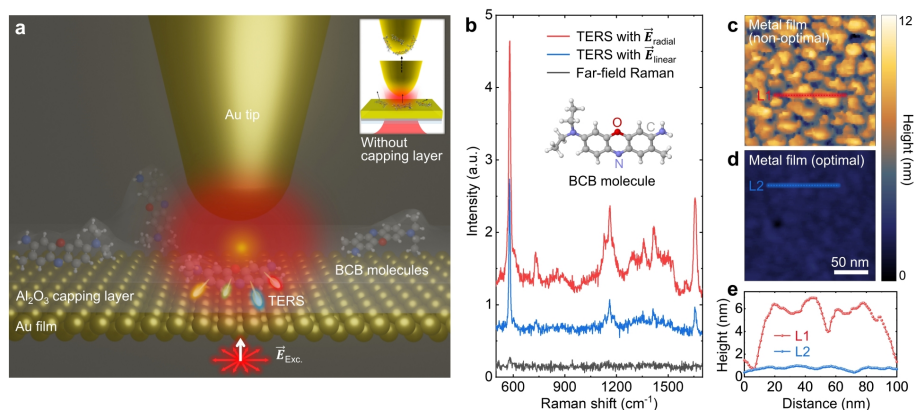


**Fig. 1** (a) Schematic illustration of bottom-illumination mode TERS. The encapsulated BCB molecules on the Au surface are excited by a radially polarized beam ( $\vec{E}_{Exc}$ ) and the back-scattered TERS responses are collected. The inset illustration shows a tip-contamination process in conventional TERS without using a Al<sub>2</sub>O<sub>3</sub> capping layer. (b) Far-field (black) and TERS spectra with different excitation polarization conditions. The TERS response with the radially polarized excitation laser (red) gives a larger enhancement compared to that obtained with the linearly polarized laser (blue). (c, d) AFM topography images of thin metal films fabricated with different deposition rates and cleaning methods of the substrate (coverslip). The coverslip for the non-optimal metal film (c) is cleaned using piranha solution, and the metal film is fabricated with a deposition rate of 0.01 nm/s. By contrast, the coverslip for the optimal metal film (d) is cleaned by ultrasonication in acetone and isopropyl alcohol along with O<sub>2</sub> plasma, and the metal film is fabricated with a deposition rate of 0.1 nm/s. (e) Topographic line profiles of two thin metal films, derived from (c) and (d).

(see Fig. S2 for the TERS background). With the exposure time of 0.5 s, we hardly observed the far-field Raman response of molecules (black), due to the extremely low Raman scattering cross-section. By contrast, we observed a few distinct Raman modes via the TERS measurements with a linearly polarized excitation (blue). Moreover, through the radially polarized excitation,<sup>47,48</sup> we observed most of the normal modes with a substantially larger TERS intensity (red) compared to the TERS spectra measured with the linearly polarized excitation. Because the radially-polarized beam has much larger vertical field component after passing through a high NA objective lens compared to the linearly-polarized beam.<sup>49</sup> For example, the C-H<sub>2</sub> scissoring mode at  $\sim 1360$  cm<sup>-1</sup> is clearly identified in the TERS spectrum measured with the radially polarized light, whereas it is not present in the TERS spectrum measured with the linearly polarized light.

**Optimization of the metal substrate for TERS.** In bottom-illumination mode TERS, the deposition of flat thin metal films on the coverslip is required to preserve the transparency of the substrate and to avoid SERS and fluorescence signals originating from the metal nano-structures. To demonstrate the influence of the surface condition of metal films, we performed a control experiment based on Au films fabricated by four different conditions with two control parameters of the cleaning method and the deposition rate (see Table S1 for detailed control parameters). From the AFM



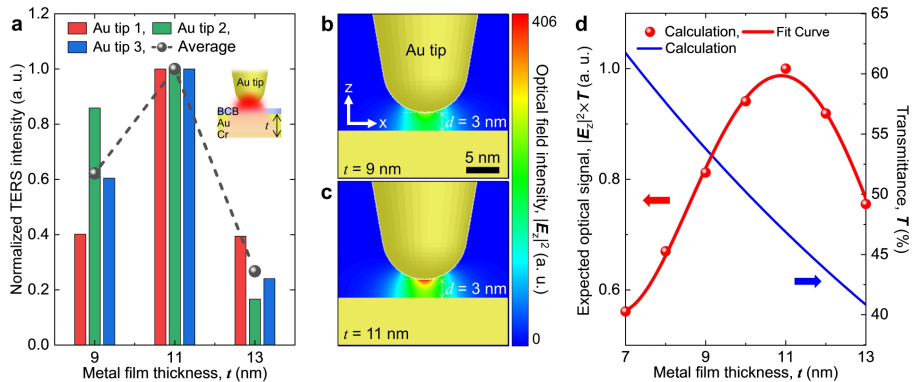


**Fig. 2** (a) Comparison of TERS intensity of BCB molecules for the metal substrates with different thicknesses ( $t = 9, 11$ , and  $13$  nm). The ratio of tip-enhanced and tip-retracted Raman intensities of the  $\sim 580$   $\text{cm}^{-1}$  peak is measured for different substrates with three different tips. The obtained intensity ratios for the three different tips are normalized to  $[0, 1]$  for comparison of the thickness effect. The black circles show average values for three tips. (b, c) FDTD-simulated optical field intensity ( $|\mathbf{E}_z|^2$ ) distribution at the nano-gap between the Au tip and the thin metal film with a film thickness of  $9$  nm (b) and  $11$  nm (c). (d) Expected optical signal (red) in the bottom-illumination mode and theoretically calculated transmittance (blue) with respect to the thickness of the metal film. The expected optical signal is calculated by the FDTD-simulated optical field intensity at the nano-gap multiplied by transmittance ( $T$ ) at each film thickness. The derived result of the expected optical signal as a function of the metal film thickness is fit with a nonlinear curve (red line).

results of Fig. 1c-e, we verify that the optimal process is required for fabrication of flat metal thin films (see Fig. S3 for detailed experiment results).

Another important parameter for bottom-illumination mode TERS is the metal film thickness, because a sufficiently thick metal film is required to induce strong dipole-dipole interactions between the tip dipole and the mirror dipole of the metal film.<sup>50</sup> However, the light transmission decreases with increasing metal thickness, which gives rise to a reduced excitation rate and collection efficiency in TERS. To experimentally determine the optimal thickness, we deposited Au films on  $\text{O}_2$ -plasma-cleaned coverslips with a Cr adhesion layer. We prepared six metal films with various thicknesses of  $5, 7, 9, 11, 13$ , and  $15$  nm. Among these metal substrates, we could not perform TERS experiments with the  $15$  nm metal film because it was difficult to align the tip apex to the laser focus due to low light transmission. Regarding the  $5$  and  $7$  nm metal films, we could barely observe TERS signals from the BCB film because the TERS enhancement factor was too low. Therefore, we performed a control experiment with three different metal substrates, namely with metal thicknesses of  $t = 9, 11$ , and  $13$  nm.

To compare the relative TERS intensities of BCB film for these three metal substrates, we obtained the TERS spectra for these substrates with three different Au tips, i.e., each sample was measured using three Au tips. Fig. 2a shows a comparison of the measured TERS intensities with respect to the thickness of the metal films. We consider the strongest TERS peak at  $\sim 580$   $\text{cm}^{-1}$  and determine the relative TERS intensities for different metal films. When we used three different tips for this control experiment, the TERS enhancement factors in each case were different; nevertheless,

the metal film with 11 nm thickness yielded the strongest TERS signal for all the tips. Therefore, we normalize the TERS intensity measured for the 11 nm metal film to [0, 1] for all three tips and compare the relative TERS intensities measured for the 9 and 13 nm metal films for each tip, as displayed in Fig. 2a. The black circles indicate the average TERS intensities for the three tips, for each substrate. The TERS intensities of the  $\sim 580\text{ cm}^{-1}$  peak, measured for the 9 nm and 13 nm thick metal films, are  $\sim 30\%$  and  $\sim 60\%$  lower than that measured for the 11 nm metal film.

We then verified the ideal metal film thickness through theoretical approaches. First, we calculated the localized optical field intensity between the Au tip apex and the Au surface with respect to the metal film thickness using finite-difference time-domain (FDTD) simulations under the excitation light sources ( $\lambda = 632.8\text{ nm}$ ) placed below the Au film (see Methods and Fig. S4 for details). Fig. 2b and c show the simulated  $|E_z|^2$  distributions for the metal film thicknesses of 9 nm and 11 nm, respectively (see Fig. S5 for  $|E_x|^2$  and  $|E_{total}|^2$  components). When we set the distance  $d$  between the Au tip and Au surface to  $d = 3\text{ nm}$  (i.e., the expected gap in tuning fork-based AFM), we achieve the maximum excitation rate for TERS,  $|E_z|^2 \approx 400$ , with the metal thickness of 11 nm. Fig. 2d shows the expected optical signal ( $|E_z|^2 \times T$ , where  $T$  is the calculated transmittance at  $\lambda \sim 657\text{ nm}$  by considering the strongest Raman peak of BCB at  $\sim 580\text{ cm}^{-1}$ , as shown in Fig. S6) as a function of the metal film thickness in the bottom-illumination geometry.  $T$  is calculated with the following formula:<sup>51</sup>

$$T = \left| \frac{E(t)}{E_0} \right|^2 = e^{-4\pi\kappa t/\lambda}, \quad (1)$$

where  $E_0$  and  $E(t)$  are incident and transmitted optical field amplitudes,  $\kappa$  is the extinction coefficient of Au at the given wavelength  $\lambda$ , and  $t$  is the thickness of the metal film (see also Fig. S7 for the experimentally measured transmittance).<sup>52</sup>  $|E_z|^2$  at each film thickness is obtained from FDTD simulations and multiplied by  $T$ , as the light passes through the metal film.  $|E_z|^2 \times T$  is gradually enhanced with an increase in thickness up to  $t = 11\text{ nm}$ , but interestingly, it starts to decrease from 12 nm. To understand this behavior, we performed the same thickness-dependence simulations for different gaps between the tip and the metal surface (see Fig. S8 for simulated results). Through these simulations, we found that the optimal metal film thickness varies slightly depending on the gap; nevertheless, the optimal metal film thickness is  $\sim 11 - 12\text{ nm}$  irrespective of the tip-surface gap (see also Fig. S9 for the effect of  $\text{Al}_2\text{O}_3$  at the tip-sample junction). Note that a previous study demonstrated that the plasmon resonance from a  $\sim 12\text{ nm}$  thick Au film gives rise to the largest TERS enhancement for the optical responses at  $\sim 640\text{ nm}$ .<sup>53</sup> Through the optimization process, the estimated TERS enhancement factor in our experiment is  $\sim 2.0 \times 10^5$  (see Supplementary Information for details), which is sufficient for single-molecule level Raman scattering detection as discussed in the previous study.<sup>54</sup>

**Single-molecule level TERS imaging at room temperature.** We then performed the hyperspectral TERS imaging of single isolated BCB molecules adsorbed on the optimal metal film ( $t = 11\text{ nm}$ ). First of all, we prepared a low-molecular density sample as described in Methods. Then, the freeze-frame (0.5 nm thick  $\text{Al}_2\text{O}_3$ ) allowed

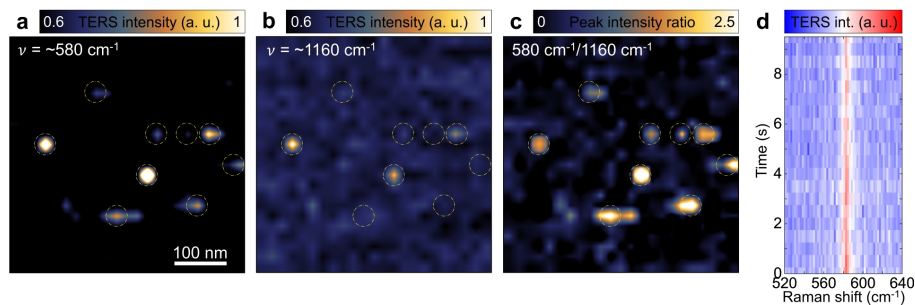


**Fig. 3** TERS mapping images of single BCB molecules measured with the excitation laser power of 220  $\mu\text{W}$  and acquisition time of 0.5 s at each pixel at room temperature. TERS peak intensity images for in-plane symmetric stretching mode of O-C<sub>2</sub> and N-C<sub>2</sub> observed at  $\sim 580 \text{ cm}^{-1}$  (a) and in-plane asymmetric stretching mode of O-C<sub>2</sub> observed at  $\sim 1160 \text{ cm}^{-1}$  (b). (c) TERS peak-to-peak intensity ratio image of  $\sim 580 \text{ cm}^{-1}$  and  $\sim 1160 \text{ cm}^{-1}$  peaks, arithmetically calculated from TERS images (a) and (b) after filtering a background fluorescence signal. Yellow dashed circles in (a-c) indicate the same positions in the TERS images. (d) Time-series TERS spectra at a single fixed position.

us to stably detect single-molecule responses at room temperature (see Methods for details). Fig. 3a and b show the TERS integrated intensity images of the vibrational modes at  $\sim 580 \text{ cm}^{-1}$  (in-plane stretching mode of C and O atoms in the middle of the molecule) and  $\sim 1160 \text{ cm}^{-1}$  (in-plane asymmetric stretching mode of O atom), which are only two recognizable TERS peaks of a single or a few BCB molecules, due to the short acquisition time (0.5 s) in our TERS mapping<sup>30,41</sup> (see also Fig. S10 for the raw images of Fig. 3a and b). In the TERS images of both the  $\sim 580 \text{ cm}^{-1}$  and the  $\sim 1160 \text{ cm}^{-1}$  modes, the TERS intensity of the detected regions shows a spatial variation even though the responses are detected in similar nanoscale areas. This spatially heterogeneous intensity distribution originates from the difference in the number of probing molecules and/or the molecular orientation on the Au surface. Since the apex size of the electrochemically etched Au tip is larger than  $\sim 15 \text{ nm}$ , several molecules under the tip can be detected together, which gives rise to a strong TERS response. Alternatively, although some of the observed TERS responses are from single molecules, the Raman scattering cross-section can differ from molecule to molecule due to their orientations and the corresponding TERS selection rule.<sup>5</sup> Specifically, because the excitation field in our TERS setup has a strong out-of-plane polarization component, the peak-to-peak Raman scattering intensity changes depending on the conformation of a molecule. Hence, the conformational heterogeneity of probed molecules can be best exemplified by the peak intensity ratio of the vibrational modes at  $\sim 580 \text{ cm}^{-1}$  (Fig. 3a) and the  $\sim 1160 \text{ cm}^{-1}$  (Fig. 3b), as shown in Fig. 3c. As previously mentioned, since TERS tip selectively probes the out-of-plane modes with respect to the surface, the peak intensity ratio can be low for multiple molecules in comparison with the single molecules. It should be noted that any structural evidence of single molecules was not found in the simultaneously measured AFM topography image (Fig. S11). Fig. 3d shows time-series TERS spectra at a single spot exhibiting robust signals without spectral fluctuations owing to the freeze-frame effect. From this result, we expect stationary conformation of the molecules in

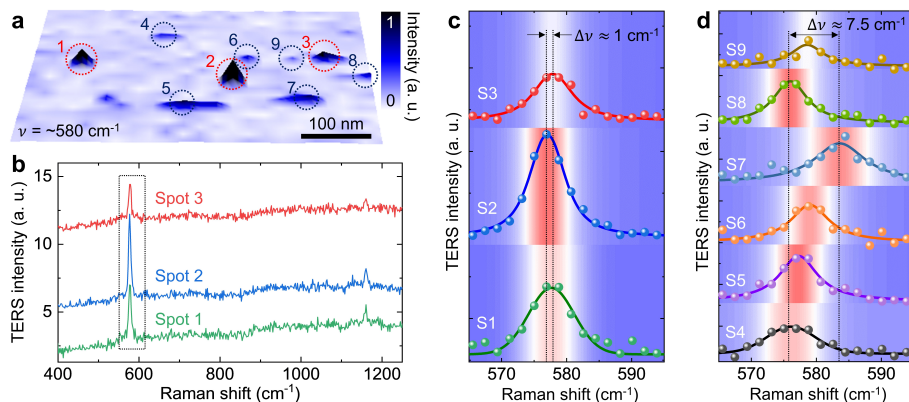


**Fig. 4** (a) TERS peak intensity image of the vibrational mode at  $\sim 580 \text{ cm}^{-1}$  of BCB molecules. (b) TERS spectra measured at spots 1, 2 and 3 indicated with red circles in (a). TERS spectra measured at spots 1-3 (c) and spots 4-9 (d) fitted with the Voigt line shape function in the range from  $565 \text{ cm}^{-1}$  to  $595 \text{ cm}^{-1}$ . From the observed TERS peak shift in Fig. 4d, the TERS spectra at spots 1-3 (red circles in Fig. 4a) are probably measured from molecule ensembles and spots 4-9 (dark blue circles in Fig. 4a) are possibly measured from molecule single or a few molecules. In Fig. 4c and d, the dots and lines are experimental data and fitted curves, and the TERS spectra at each spot are also shown as background 2D contour images.

the measurement area of Fig. 3a-c. By contrast, fluctuating TERS spectra with respect to time are observed without the capping layer (see Fig. S12 for comparison).

From the TERS response corresponding to the nanoscale regions in the TERS image, we can infer the possibility of single-molecule detection; nevertheless, more substantial evidence is needed to verify this possibility. In addition to the aforementioned molecular orientation and the selection rule, the vibrational energy of the normal modes of an adsorbed molecule can change due to coupling with the atoms of the metal surface, leading to peak shift and intensity change signatures.<sup>4,55,56</sup> Additionally, the peak linewidth should be considered to distinguish the molecular ensembles from the single or a few molecules.<sup>29</sup> Further, to distinguish the single, a few, or multiple molecules, we also need to consider the spatial distribution in TERS images in addition to spectroscopic information.<sup>57</sup> Hence, we analyze the spectral properties and spatial distribution of the observed spots in the TERS image to obtain the evidence of single-molecule detection. First, we classify the observed TERS spots in Fig. 3 into two groups, as shown in Fig. 4a. We surmise that the TERS response in the first group (red circled spots 1-3) was measured from multiple BCB molecules because the TERS signal of both the  $\sim 580 \text{ cm}^{-1}$  and the  $\sim 1160 \text{ cm}^{-1}$  modes are pronounced and significant TERS peak shift is not observed with generally broad linewidth, as shown in Fig. 4b and c (see also Fig. 3a and b). By contrast, we observe much weaker TERS responses in the second group (blue circled spots 4-9 in Fig. 4a) with a significant peak variation corresponding to  $\sim 580 \text{ cm}^{-1}$ , as large as  $\sim 7.5 \text{ cm}^{-1}$ , as shown in Fig. 4d (see Fig. S13 for the full spectra). We then consider the linewidth of each spectrum and spatial distribution in the TERS image to distinguish the single and a few molecules. First of all, we classify the spot 4 as a few molecules. Although its TERS intensity is weak with the small spatial distribution, the linewidth is quite broad ( $7.5 \text{ cm}^{-1}$ ) comparable to the first group (see Table S2 for details). It should be

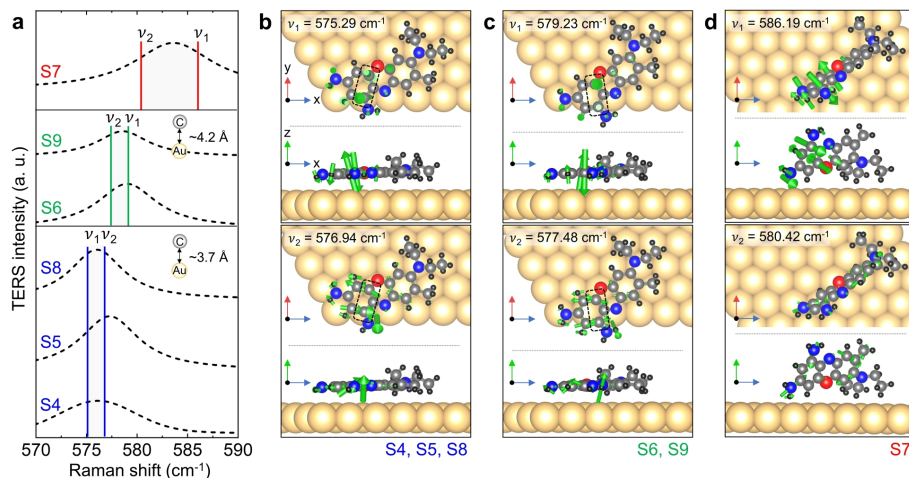


**Fig. 5** (a) The measured TERS spectra (dashed curves) derived from Fig. 4d and DFT-calculated normal modes (colored vertical lines) for different chemical environments and molecular orientations. (b-d) Models of a BCB molecule on the Au surface for the DFT calculations of normal modes in different conditions exhibiting the origin of the observed peak shift of single-molecule TERS measurements.

noted that a few molecules can show broad linewidth even with double peaks when the molecules have different conformations (see Fig. S14 for details). The remaining five spots (S5-9) show narrow linewidths of  $\leq 6.0 \text{ cm}^{-1}$ , which is closer to the spectral resolution in our experiment (see also Fig. S12). Hence, we finally classify these spots into single or a few molecules group based on the spatial distribution in TERS image. As can be seen in Fig. 4a, the TERS response of spots S5, S7, and S8 is spatially spread out, which means the signals were obtained from a few molecules. Therefore, from the spatio-spectral analyses, we believe the TERS responses from S6 and S9 are possibly originated from single isolated BCB molecules.

**DFT calculation of vibrational modes in different chemical environments.** To reveal the possible origins of the observed TERS peak variations, we calculated the normal vibrational modes of a BCB molecule through DFT simulations. It should be noted that why we exclude other possible effects of the observed spectral shifts. First, spectral shifts can occur depending upon the chemically distinct states, i.e., protonation and deprotonation, of molecules due to the local pH differences.<sup>58</sup> However, in our work, the spin-coated BCB molecules are physisorbed on the Au surface (not chemical binding) and the proton transfer process is rarely occurred because of the encapsulating dielectric layer on the molecules.<sup>59</sup> Second, spectral shifts can be observed by the hot-carrier injection from the plasmonic metal to molecules because it can cause a change in molecular bond lengths.<sup>60</sup> However, in our experiment, we could exclude this hot-carrier injection effect because the tip-molecule distance is maintained to  $\sim 3 \text{ nm}$  and the dielectric capping layer also suppresses the hot-carrier injection. Third, a previous study demonstrated that oxidation-reduction reaction of molecules could be induced by electrochemical TERS.<sup>61</sup> However, since we do not

apply external bias to the BCB molecules, we believe the redox effect is negligible in our observed spectral shifts. Lastly for the possibility of the Stark effect, it was experimentally observed for single molecules sandwiched with the metal nano-gap when the applied DC electric fields at the gap was large enough ( $\sim 10$  V/nm).<sup>62</sup> On the other hand, since we do not apply external bias to the BCB molecules, we could ignore the Stark effect.

Since the BCB molecules are encapsulated using a thin dielectric layer, we presume the spectral diffusion is suppressed, as experimentally demonstrated in Fig. 3d. Based on this assumption, we design two kinds of fixed conformations of a BCB molecule, i.e., horizontal and vertical geometries with respect to the Au (111) surface. Regarding horizontally laying molecules, we additionally consider the position of the BCB molecules (especially C atoms vibrating with a large amplitude for the  $\sim 580$   $\text{cm}^{-1}$  mode) with respect to the Au atoms since the substrate-molecule coupling effect can be slightly changed (see Methods for calculation details).

Fig. 5a shows the calculated normal modes (colored vertical lines) of a BCB molecule with the measured TERS spectra at spots 4-9 (from Fig. 4a and d) for different chemical environments described in Fig. 5b-d. In the frequency range of 570 - 590  $\text{cm}^{-1}$ , two theoretical vibrational modes ( $\nu_1$  and  $\nu_2$ ) are observed even though only a single peak was experimentally observed due to the limited spectral resolution and inhomogeneous broadening at room temperature. As individual atoms in a BCB molecule involve additional coupling to Au atoms on the surface, the Raman frequencies of two vibrational modes are varied depending on the conformation and the position of the molecule. When the two strongly oscillating C atoms of the molecule (as indicated with black dashed rectangles in Fig. 5b) are closer to the nearest Au atoms (the average atomic distance of two carbon atoms with the Au atom is 3.7 Å),  $\nu_1$  is calculated as 575.29  $\text{cm}^{-1}$  with the out-of-plane bending vibration mode of the C atoms and  $\nu_2$  is calculated as 576.94  $\text{cm}^{-1}$  with the in-plane stretching mode of the C atoms. By contrast, when these C atoms (as indicated with black dashed rectangles in Fig. 5c) are vertically mis-located with longer atomic distance with respect to the Au atoms (the average atomic distance of two carbon atoms with the Au atom is 4.2 Å), the Raman frequency of the out-of-plane bending mode of the C atoms is increased to 579.23  $\text{cm}^{-1}$  ( $\nu_1$  in Fig. 5c). It is likely that the two strongly oscillating C atoms having shorter atomic distance with the Au atoms (Fig. 5b) experience stronger damping forces than the C atoms located further away from the closest Au atoms (Fig. 5c). On the other hand, both  $\nu_1$  and  $\nu_2$  are significantly increased for a vertically standing molecule (Fig. 5d) due to the lessened molecular coupling with the Au atoms (see Fig. S15 for the normal mode of a BCB molecule in the gas phase).

From these simulation results, we can deduce that the experimentally observed possible single molecules in S6, and S9 (in Fig. 3 and 4) probably have similar molecular orientations to the illustrations in Fig. 5c. Because the other chemical or environmental conditions give much less effect to the spectral shift compared to the molecular orientation and coupling (mainly C - Au atoms) as we discussed previously.



The observed molecule in S8 is expected to have same molecular orientation as the molecules in S4, and S5 with the C atoms vertically aligned with respect to the Au atoms, as shown in Fig. 5b. The observed broader linewidth and higher frequency TERS peak at S7 indicate the molecule in S7 is oriented vertically, as displayed in Fig. 5d. Hence, in this work, we experimentally verified the freeze-frame effect using a thin dielectric layer and probed the conformational heterogeneity of possible single molecules at room temperature through highly sensitive TERS imaging and spectral analyses with DFT simulations.

## Conclusion

In summary, we demonstrated the hyperspectral TERS imaging of possibly single molecules at room temperature by optimizing experimental conditions. In addition, the thin dielectric Al<sub>2</sub>O<sub>3</sub> layer encapsulating the single molecules adsorbed onto the Au (111) surface played a significant role, as a freeze-frame, in enabling room temperature single-molecule TERS imaging. This is because the thin dielectric layer can suppress the rotational and spectral diffusions of molecules and inhibit the chemical reactions and contaminations in air, including potential physisorption of molecules onto the Au tip.<sup>63,64</sup> Through this room-temperature TERS imaging approach at the single-molecule level, we examined the conformational heterogeneity of BCB molecules with supporting theoretical DFT calculations. We envision that the presented optimal experimental setup for single-molecule TERS measurements will be broadly exploited to investigate unrevealed single-molecule characteristics at room temperature. For example, we can investigate intramolecular vibrational relaxation (IVR) more accurately at the single-molecule level using this freeze-frame and variable-temperature TERS.<sup>5</sup> In addition, the single-molecule strong coupling study at room temperature will be more easily accessible and various advanced studies will be enabled,<sup>6</sup> such as tip-enhanced plasmon-phonon strong coupling and investigation of the coupling strength with respect to the molecular orientation. Furthermore, this approach can extend to the single-molecule transistor studies at room temperature with very robust conditions.

## Methods

**Sample preparation:** Coverslips (thickness: 170  $\mu\text{m}$ ) for non-optimal metal films (Fig. 1c) were cleaned with piranha solution (3:1 mixture of H<sub>2</sub>SO<sub>4</sub> and H<sub>2</sub>O<sub>2</sub>) for > 60 mins and ultrasonicated in deionized water. The other coverslips for optimal metal films (Fig. 1d) were ultrasonicated in acetone and isopropanol for 10 mins each, followed by O<sub>2</sub> plasma treatment for 10 mins. The coverslips were then deposited with a Cr adhesion layer with a thickness of 2 nm (a rate of 0.01 nm/s) and subsequently deposited with Au films with varying thicknesses (0.01 nm/s to 0.1 nm/s) at the base pressure of  $\sim 10^{-6}$  torr using a conventional thermal evaporator. The deposition rate of metals was precisely controlled using a quartz crystal microbalance (QCM) detector. The transmittance spectra of the substrates were measured by a UV-Vis spectrometer (UV-1800, Shimadzu). Next, BCB molecules in ethanol solution (100 nM for the single-molecule experiment and 1.0 mM for the thickness optimization process) were



spin-coated on the metal thin films at 3000 rpm. Finally, an Al<sub>2</sub>O<sub>3</sub> capping layer with a thickness of 0.5 nm was deposited on the sample surface using an atomic layer deposition system (Lucida D100, NCD Co.). The Al<sub>2</sub>O<sub>3</sub> layer was deposited with the growth rate of 0.11 nm per cycle at the temperature of 150 °C under the base pressure of 40 mTorr. Precursor for the Al<sub>2</sub>O<sub>3</sub> ALD was trimethylaluminum (TMA) vapor, and H<sub>2</sub>O vapor as the oxidant with N<sub>2</sub> carrier gas.

**TERS imaging setup:** For TERS experiments, we used a commercial optical spectroscopy system combined with an AFM (NTEGRA Spectra II, NT-MDT). The excitation beam from a single-mode-fiber-coupled He-Ne laser ( $\lambda = 632.8$  nm, optical power  $P$  of  $\geq 1$  mW) passed through a half-wave plate ( $\lambda/2$ ) and was collimated using the two motorized lenses. The beam passed through a radial polarizer and was focused onto the sample surface with an oil immersion lens (NA = 1.3, RMS100X-PFOD, Olympus) in the inverted optical microscope geometry. The electrochemically etched Au tip (apex radius of  $\sim 10$  nm) attached on a tuning fork was controlled using a PZT scanner to alter the position of the Au tip with respect to the focused laser beam. The backscattered signals were collected through the same optics and transmitted to a spectrometer and charge-coupled device (Newton, Andor) after passing through an edge filter (633 nm cut off). The spectrometer was calibrated using a mercury lamp and the Si Raman peak at  $520\text{ cm}^{-1}$ , and its spectral resolution was  $\sim 4.3\text{ cm}^{-1}$  for a 600 g/mm grating.

**FDTD simulation of optical field distribution:** We used finite-domain time-difference (FDTD) simulations (Lumerical Solutions, Inc.) to quantify the optical field enhancement at the apex of the Au tip with respect to the metal film thickness. The distance between the Au tip and the Au film was set to 2 - 4 nm based on our experimental condition. As a fundamental excitation source, monochromatic 632.8 nm light was used with linear polarization parallel to the tip axis. The theoretical transmittance of thin gold films was calculated using the material properties obtained from Olmon *et al.*<sup>52</sup>

**DFT calculation of BCB vibrational modes:** DFT calculations were performed using the Vienna Ab initio Simulation Package (VASP) to identify the normal vibrational modes of a single BCB molecule. In our simulation model, the chemical environment and molecular orientation were critically considered; i.e., the vibrational modes for a BCB molecule placed in a free space and adsorbed onto the Au (111) surface in different orientations and positions were calculated. Specifically, molecules oriented normal and parallel to the Au surface were modeled. For a molecule placed parallel to the Au surface, the lateral position was varied, as shown in Fig. 5, to consider the effect of an interaction between the atoms of the BCB molecule and those of the Au surface. To describe the adsorption of a molecule on the Au (111) surface, Tkatchenko and Scheffler (TS) dispersion correction<sup>65</sup> with

the Perdew-Burke-Ernzerhof (PBE) exchange functional<sup>66</sup> was employed. Regarding the Au (111) slab supercell, four layers of Au atoms were considered, with the top two layers optimized in the gamma point. Furthermore, 1.5 nm vacuum space was considered to avoid an interaction between periodic slabs, and the plane-wave energy cutoff was set to 550 eV. The vibrational modes of the BCB molecule were shown using visualization for electronic and structural analysis (VESTA).

## Data Availability

The data that support the findings of this study are available from the corresponding author upon reasonable request.

## References

- [1] Nie, S. & Emory, S. R. Probing single molecules and single nanoparticles by surface-enhanced raman scattering. *science* **275**, 1102–1106 (1997).
- [2] Kneipp, K. *et al.* Single molecule detection using surface-enhanced raman scattering (sers). *Physical Review Letters* **78**, 1667–1670 (1997). URL <https://dx.doi.org/10.1103/physrevlett.78.1667>.
- [3] Vosgröne, T. & Meixner, A. Surface-and resonance-enhanced micro-raman spectroscopy of xanthene dyes: from the ensemble to single molecules. *ChemPhysChem* **6**, 154–163 (2005).
- [4] Sonntag, M. D., Chulhai, D., Seideman, T., Jensen, L. & Van Duyne, R. P. The origin of relative intensity fluctuations in single-molecule tip-enhanced raman spectroscopy. *Journal of the American Chemical Society* **135**, 17187–17192 (2013). URL <https://dx.doi.org/10.1021/ja408758j>.
- [5] Park, K. D. *et al.* Variable-temperature tip-enhanced raman spectroscopy of single-molecule fluctuations and dynamics. *Nano Letters* **16**, 479–87 (2016). URL <https://www.ncbi.nlm.nih.gov/pubmed/26679007>.
- [6] Chikkaraddy, R. *et al.* Single-molecule strong coupling at room temperature in plasmonic nanocavities. *Nature* **535**, 127–130 (2016). URL <https://doi.org/10.1038/nature17974>.

- [7] Pozzi, E. A. *et al.* Evaluating single-molecule stokes and anti-stokes sers for nanoscale thermometry. *The Journal of Physical Chemistry C* **119**, 21116–21124 (2015).
- [8] Chiang, N. *et al.* Conformational contrast of surface-mediated molecular switches yields ångstrom-scale spatial resolution in ultrahigh vacuum tip-enhanced raman spectroscopy. *Nano letters* **16**, 7774–7778 (2016).
- [9] Kleinman, S. L. *et al.* Single-molecule surface-enhanced raman spectroscopy of crystal violet isotopologues: theory and experiment. *Journal of the American Chemical Society* **133**, 4115–4122 (2011).
- [10] Zhang, Y. *et al.* Coherent anti-stokes raman scattering with single-molecule sensitivity using a plasmonic fano resonance. *Nature communications* **5**, 1–7 (2014).
- [11] Griffiths, J. *et al.* Resolving sub-ångstrom ambient motion through reconstruction from vibrational spectra. *Nature communications* **12**, 1–8 (2021).
- [12] Palings, I. *et al.* Assignment of fingerprint vibrations in the resonance raman spectra of rhodopsin, isorhodopsin, and bathorhodopsin: implications for chromophore structure and environment. *Biochemistry* **26**, 2544–2556 (1987). URL <https://dx.doi.org/10.1021/bi00383a021>.
- [13] Hiura, H., Ebbesen, T. W., Tanigaki, K. & Takahashi, H. Raman studies of carbon nanotubes. *Chemical Physics Letters* **202**, 509–512 (1993). URL [https://dx.doi.org/10.1016/0009-2614\(93\)90040-8](https://dx.doi.org/10.1016/0009-2614(93)90040-8).
- [14] Stöckle, R. M., Suh, Y. D., Deckert, V. & Zenobi, R. Nanoscale chemical analysis by tip-enhanced raman spectroscopy. *Chemical Physics Letters* **318**, 131–136 (2000). URL [https://dx.doi.org/10.1016/S0009-2614\(99\)01451-7](https://dx.doi.org/10.1016/S0009-2614(99)01451-7).
- [15] Jiang, N. *et al.* Tip-enhanced raman spectroscopy: From concepts to practical applications. *Chemical Physics Letters* **659**, 16–24 (2016).
- [16] Verma, P. Tip-enhanced raman spectroscopy: Technique and recent advances. *Chemical Reviews* **117**, 6447–6466 (2017). URL <https://dx.doi.org/10.1021/acs.chemrev.6b00821>.
- [17] Pszona, M., Gawinkowski, S., Jäger, R., Kamińska, I. & Waluk, J. Influence of bulky substituents on single-molecule sers sensitivity. *The Journal of Chemical Physics* **156**, 014201 (2022).
- [18] Zhang, R. *et al.* Chemical mapping of a single molecule by plasmon-enhanced raman scattering. *Nature* **498**, 82–86 (2013). URL <https://dx.doi.org/10.1038/nature12151>.

- [19] Zhang, Y., Zhang, R., Jiang, S., Zhang, Y. & Dong, Z.-C. Probing adsorption configurations of small molecules on surfaces by single-molecule tip-enhanced raman spectroscopy. *ChemPhysChem* **20**, 37–41 (2019). URL <https://dx.doi.org/10.1002/cphc.201800861>.
- [20] Lee, J., Crampton, K. T., Tallarida, N. & Apkarian, V. A. Visualizing vibrational normal modes of a single molecule with atomically confined light. *Nature* **568**, 78–82 (2019). URL <https://dx.doi.org/10.1038/s41586-019-1059-9>.
- [21] Jaculbia, R. B. *et al.* Single-molecule resonance raman effect in a plasmonic nanocavity. *Nature Nanotechnology* **15**, 105–110 (2020). URL <https://dx.doi.org/10.1038/s41565-019-0614-8>.
- [22] Liu, S. *et al.* Resolving the correlation between tip-enhanced resonance raman scattering and local electronic states with 1 nm resolution. *Nano Letters* **19**, 5725–5731 (2019). URL <https://dx.doi.org/10.1021/acs.nanolett.9b02345>.
- [23] Liu, S. *et al.* Dramatic enhancement of tip-enhanced raman scattering mediated by atomic point contact formation. *Nano Letters* **20**, 5879–5884 (2020). URL <https://dx.doi.org/10.1021/acs.nanolett.0c01791>.
- [24] Bhattarai, A., Joly, A. G., Hess, W. P. & El-Khoury, P. Z. Visualizing electric fields at au(111) step edges via tip-enhanced raman scattering. *Nano Letters* **17**, 7131–7137 (2017). URL <https://dx.doi.org/10.1021/acs.nanolett.7b04027>.
- [25] Kawata, S., Inouye, Y. & Verma, P. Plasmonics for near-field nano-imaging and superlensing. *Nature Photonics* **3**, 388–394 (2009). URL <https://dx.doi.org/10.1038/nphoton.2009.111>.
- [26] Jiang, N. *et al.* Observation of multiple vibrational modes in ultrahigh vacuum tip-enhanced raman spectroscopy combined with molecular-resolution scanning tunneling microscopy. *Nano letters* **12**, 5061–5067 (2012).
- [27] Klingsporn, J. M. *et al.* Intramolecular insight into adsorbate–substrate interactions via low-temperature, ultrahigh-vacuum tip-enhanced raman spectroscopy. *Journal of the American Chemical Society* **136**, 3881–3887 (2014). URL <https://dx.doi.org/10.1021/ja411899k>.
- [28] Kong, F.-F. *et al.* Probing intramolecular vibronic coupling through vibronic-state imaging. *Nature communications* **12**, 1–8 (2021).
- [29] Artur, C., Le Ru, E. C. & Etchegoin, P. G. Temperature dependence of the homogeneous broadening of resonant raman peaks measured by single-molecule surface-enhanced raman spectroscopy. *The Journal of Physical Chemistry Letters* **2**, 3002–3005 (2011). URL <https://dx.doi.org/10.1021/jz2013787>.

- [30] Steidtner, J. & Pettinger, B. Tip-enhanced raman spectroscopy and microscopy on single dye molecules with 15 nm resolution. *Physical Review Letters* **100**, 236101 (2008). URL <https://dx.doi.org/10.1103/PhysRevLett.100.236101>.
- [31] Neugebauer, U. *et al.* On the way to nanometer-sized information of the bacterial surface by tip-enhanced raman spectroscopy. *Chemphyschem: a European journal of chemical physics and physical chemistry* **7**, 1428–1430 (2006).
- [32] van Schrojenstein Lantman, E. M., Deckert-Gaudig, T., Mank, A. J., Deckert, V. & Weckhuysen, B. M. Catalytic processes monitored at the nanoscale with tip-enhanced raman spectroscopy. *Nature nanotechnology* **7**, 583–586 (2012).
- [33] Zhang, Y. *et al.* Visually constructing the chemical structure of a single molecule by scanning raman picoscopy. *National Science Review* **6**, 1169–1175 (2019).
- [34] Liu, Q. *et al.* Hypericin: Single molecule spectroscopy of an active natural drug. *The Journal of Physical Chemistry A* **124**, 2497–2504 (2020). URL <https://dx.doi.org/10.1021/acs.jpca.9b11532>.
- [35] De Albuquerque, C. D. L. & Schultz, Z. D. Super-resolution surface-enhanced raman scattering imaging of single particles in cells. *Analytical Chemistry* **92**, 9389–9398 (2020). URL <https://dx.doi.org/10.1021/acs.analchem.0c01864>.
- [36] Schuler, B., Lipman, E. A. & Eaton, W. A. Probing the free-energy surface for protein folding with single-molecule fluorescence spectroscopy. *Nature* **419**, 743–747 (2002). URL <https://dx.doi.org/10.1038/nature01060>.
- [37] Bustamante, C., Alexander, L., Maciuba, K. & Kaiser, C. M. Single-molecule studies of protein folding with optical tweezers. *Annual Review of Biochemistry* **89**, 443–470 (2020). URL <https://dx.doi.org/10.1146/annurev-biochem-013118-111442>.
- [38] Bailo, E. & Deckert, V. Tip-enhanced raman spectroscopy of single rna strands: towards a novel direct-sequencing method. *Angewandte Chemie International Edition* **47**, 1658–1661 (2008).
- [39] Mehta, A. D. Single-molecule biomechanics with optical methods. *Science* **283**, 1689–1695 (1999). URL <https://dx.doi.org/10.1126/science.283.5408.1689>.
- [40] Zhuang, X. A single-molecule study of rna catalysis and folding. *Science* **288**, 2048–2051 (2000). URL <https://dx.doi.org/10.1126/science.288.5473.2048>.
- [41] Zhang, W., Yeo, B. S., Schmid, T. & Zenobi, R. Single molecule tip-enhanced raman spectroscopy with silver tips. *The Journal of Physical Chemistry C* **111**, 1733–1738 (2007). URL <https://dx.doi.org/10.1021/jp064740r>.

- [42] Neacsu, C. C., Dreyer, J., Behr, N. & Raschke, M. B. Scanning-probe raman spectroscopy with single-molecule sensitivity. *Physical Review B* **73**, 193406 (2006).
- [43] Worley, C. G. & Linton, R. W. Removing sulfur from gold using ultraviolet/ozone cleaning. *Journal of Vacuum Science & Technology A: Vacuum, Surfaces, and Films* **13**, 2281–2284 (1995).
- [44] Comini, N., Huthwelker, T., Diulus, J. T., Osterwalder, J. & Novotny, Z. Factors influencing surface carbon contamination in ambient-pressure x-ray photoelectron spectroscopy experiments. *Journal of Vacuum Science & Technology A: Vacuum, Surfaces, and Films* **39**, 043203 (2021).
- [45] Hayazawa, N., Saito, Y. & Kawata, S. Detection and characterization of longitudinal field for tip-enhanced raman spectroscopy. *Applied Physics Letters* **85**, 6239–6241 (2004). URL <https://dx.doi.org/10.1063/1.1839646>.
- [46] Sackrow, M., Stanciu, C., Lieb, M. A. & Meixner, A. J. Imaging nanometre-sized hot spots on smooth au films with high-resolution tip-enhanced luminescence and raman near-field optical microscopy. *ChemPhysChem* **9**, 316–320 (2008).
- [47] Kazemi-Zanjani, N., Vedraïne, S. & Lagugne-Labarthe, F. Localized enhancement of electric field in tip-enhanced raman spectroscopy using radially and linearly polarized light. *Optics Express* **21**, 25271–6 (2013). URL <https://www.ncbi.nlm.nih.gov/pubmed/24150367>.
- [48] Pashaee, F., Sharifi, F., Fanchini, G. & Lagugné-Labarthe, F. Tip-enhanced raman spectroscopy of graphene-like and graphitic platelets on ultraflat gold nanoplates. *Physical Chemistry Chemical Physics* **17**, 21315–21322 (2015). URL <https://dx.doi.org/10.1039/C4CP05252H>.
- [49] Kang, H., Jia, B. & Gu, M. Polarization characterization in the focal volume of high numerical aperture objectives. *Optics Express* **18**, 10813–10821 (2010).
- [50] Wang, R., He, Z., Sokolov, A. V. & Kurouski, D. Gap-mode tip-enhanced raman scattering on au nanoplates of varied thickness. *The Journal of Physical Chemistry Letters* 3815–3820 (2020). URL <https://dx.doi.org/10.1021/acs.jpcclett.0c01021>.
- [51] Hecht, E. *Optics, 5e* (Pearson, 2002).
- [52] Olmon, R. L. *et al.* Optical dielectric function of gold. *Physical Review B* **86**, 235147 (2012). URL <https://dx.doi.org/10.1103/PhysRevB.86.235147>.
- [53] Uetsuki, K., Verma, P., Nordlander, P. & Kawata, S. Tunable plasmon resonances in a metallic nanopip–film system. *Nanoscale* **4**, 5931–5935 (2012).

- [54] Park, W.-H. & Kim, Z. H. Charge transfer enhancement in the sers of a single molecule. *Nano letters* **10**, 4040–4048 (2010).
- [55] Mažeikienė, R., Niaura, G., Eicher-Lorka, O. & Malinauskas, A. Raman spectroelectrochemical study of toluidine blue, adsorbed and electropolymerized at a gold electrode. *Vibrational Spectroscopy* **47**, 105–112 (2008).
- [56] Shin, H.-H. *et al.* Frequency-domain proof of the existence of atomic-scale sers hot-spots. *Nano Letters* **18**, 262–271 (2018). URL <https://dx.doi.org/10.1021/acs.nanolett.7b04052>.
- [57] Deckert-Gaudig, T., Taguchi, A., Kawata, S. & Deckert, V. Tip-enhanced raman spectroscopy—from early developments to recent advances. *Chemical Society Reviews* **46**, 4077–4110 (2017).
- [58] Huang, J. *et al.* Tracking interfacial single-molecule ph and binding dynamics via vibrational spectroscopy. *Science Advances* **7**, eabg1790 (2021).
- [59] Singh, P. & Deckert, V. Local protonation control using plasmonic activation. *Chemical Communications* **50**, 11204–11207 (2014).
- [60] Wang, R. *et al.* Direct experimental evidence of hot carrier-driven chemical processes in tip-enhanced raman spectroscopy (ters). *The Journal of Physical Chemistry C* **124**, 2238–2244 (2020).
- [61] Kurouski, D., Mattei, M. & Van Duyne, R. P. Probing redox reactions at the nanoscale with electrochemical tip-enhanced raman spectroscopy. *Nano letters* **15**, 7956–7962 (2015).
- [62] Giesecking, R. L., Lee, J., Tallarida, N., Apkarian, V. A. & Schatz, G. C. Bias-dependent chemical enhancement and nonclassical stark effect in tip-enhanced raman spectromicroscopy of co-terminated ag tips. *The journal of physical chemistry letters* **9**, 3074–3080 (2018).
- [63] Huang, Y.-P. *et al.* Shell-isolated tip-enhanced raman and fluorescence spectroscopy. *Angewandte Chemie* **130**, 7645–7649 (2018).
- [64] Tallarida, N., Rios, L., Apkarian, V. A. & Lee, J. Isomerization of one molecule observed through tip-enhanced raman spectroscopy. *Nano Letters* **15**, 6386–6394 (2015).
- [65] Tkatchenko, A. & Scheffler, M. Accurate molecular van der waals interactions from ground-state electron density and free-atom reference data. *Physical Review Letters* **102**, 073005 (2009). URL <https://dx.doi.org/10.1103/physrevlett.102.073005>.



- [66] Perdew, J. P., Burke, K. & Ernzerhof, M. Generalized gradient approximation made simple. *Physical Review Letters* **77**, 3865–3868 (1996). URL <https://dx.doi.org/10.1103/physrevlett.77.3865>.